DOI: 10.1002/ejic.200901169

Microwave-Hydrothermal Synthesis of Nanostructured Zinc-Copper Gallates

Franziska Conrad,[a] Ying Zhou,[a] Maxim Yulikov,[b] Kathrin Hametner,[c] Stephen Weyeneth,[d] Gunnar Jeschke,[b] Detlef Günther,[c] Jan-Dierk Grunwaldt,[e] and Greta R. Patzke*[a]

Keywords: Zinc / Copper / Gallium / Microwave chemistry / Nanoparticles / Spinel phases / Hydrothermal synthesis

Zinc gallate is an important semiconductor for manifold applications, e.g. in field emission displays or as a photocatalyst for water splitting. In addition to these interesting properties, zinc gallate is also an excellent matrix material that can be furthermore tuned through the incorporation of guest cations to form functional solid solutions with new optical and catalytic properties. We present a convenient microwave-hydrothermal synthesis of nanostructured Cu^{2+}-substituted $ZnGa_2O_4$ spinels and their characterization with respect to morphology, chemical composition, structural, magnetic and optical properties. The microwave-based approach offers a straightforward and one-step access to nanostructured zinc gallate-based materials and related compounds as a new preparative advantage. As the properties of mixed spinel-based solid solutions strongly depend on the distribution of the guest ions between the different lattice sites, we have employed a wide range of analytical techniques to investigate the physico-chemical properties of the obtained copper-containing zinc gallate materials. The element specific EXAFS analysis at the Cu *K*- and Zn *K*-edge shows a difference in the coordination environments with Zn mostly situated on the tetrahedral sites of the spinel lattice whereas Cu is located on the octahedral sites of the nanostructured $ZnGa_2O_4$:Cu^{2+} materials.

Introduction

Over the past decades, major progress has been achieved in the synthesis and design of nanostructured materials for technological applications. Oxide nanomaterials are indispensable nanotechnological building blocks: they offer an outstanding variety of structural motifs and the resulting key properties can be furthermore tuned through the synthesis of oxide solid solutions and their transformation into nanoscale dimensions.[1,2] Spinels are an important class of materials among the large family of functional oxides and zinc gallate, $ZnGa_2O_4$, is a particularly interesting representative that attracts considerable research attention. Firstly, this transparent and conductive material has a high application potential in field emission displays (FEDs), electroluminescent components (ELDs)[3,4] or in plasma display panels for novel LED technologies that are superior to the conventional light sources.[5,6] Moreover, $ZnGa_2O_4$ displays promising photocatalytic properties in the degradation of benzene[7] or methylene blue (MB)[8] as important representative compounds for environmental pollutants. Furthermore, the high potential of $ZnGa_2O_4$ materials for photocatalytic water splitting[9,10] is just being explored. Generally, control over the particle size, surface area, crystallinity and dopant content is indispensable in order to develop $ZnGa_2O_4$-based photocatalysts for urgent environmental applications. The regular and oxidation-stable spinel lattice of $ZnGa_2O_4$ is not only an ideal catalytic matrix but also very interesting from the structural point of view for the study of solid solutions and their resulting electronic properties.[11]

The optical band gap of $ZnGa_2O_4$ ranges from 4.4 to 5 eV[12] and the resulting blue emission can be shifted to green and red by doping with Mn^{2+} and Cr^{3+} ions, respectively.[3,13–15] The remarkable effect of guest cations on the optical, structural and morphological properties of mixed zinc gallates has been demonstrated in numerous works.[5,13,16–20] To the best of our knowledge, however, little is known about Cu-substituted zinc gallates and the investigation of the effect of copper substitution on the luminance and conductivity of mixed zinc gallates is one of the very few works in this direction.[20] We have now performed further studies on Cu^{2+}-substituted $ZnGa_2O_4$ spinels, because they are interesting precursors for new materials, such as nanoscale Cu catalysts centers that are embedded into a stable and inert oxide matrix.[21]

[a] Institute of Inorganic Chemistry, University of Zurich, Winterthurerstrasse 190, 8057 Zurich, Switzerland
Fax: +41-44-63-56802
E-mail: greta.patzke@aci.uzh.ch
[b] Laboratory of Physical Chemistry, ETH Zurich Wolfgang-Pauli-Strasse 10, 8093 Zurich, Switzerland
[c] Laboratory of Inorganic Chemistry, ETH Zurich Wolfgang-Pauli-Strasse 10, 8093 Zurich, Switzerland
[d] Physics Institute, University of Zurich, Winterthurerstrasse 190, 8057 Zurich, Switzerland
[e] Department of Chemical and Biochemical Engineering, Technical University of Denmark, 2800 Kgs, Denmark

Supporting information for this article is available on the WWW under http://dx.doi.org/10.1002/ejic.200901169.

The properties of zinc gallates in general are a function of their preparation and of the resulting morphology, such as nanowires,[12,22,23] polyhedron-related, rod-like or irregular shapes.[24] The prevailing synthetic approaches to pristine and substituted $ZnGa_2O_4$ materials are solid-state reactions,[5,7,13,20,25–27] sol-gel methods,[18,28,29] pulsed laser deposition techniques,[30] co-precipitation,[7] chemical transport,[31] thermal evaporation,[12,22,23,32] the Pecchini approach[19] and hydrothermal methods[24,26,27,33–37] (for a survey see Supporting Information, Table S.1). Among these techniques, hydrothermal syntheses are of special interest, because they can provide homogeneous phases and particle size distributions as well as tuneable particle morphologies in a single reaction step.[38–42] The production of metal oxides with microwave-assisted hydrothermal syntheses is even superior to conventional hydrothermal routes due to enhanced crystallization kinetics, shorter reaction times and energy saving through rapid heating of the entire reaction mixture.[43,44] Recently, the use of ionic liquids has opened up new preparative avenues[45] and microwave-hydrothermal technologies are likely to replace the conventional routes in future technical implementations.

In this study, we present a new microwave-hydrothermal synthesis of nanostructured Cu^{2+}-containing zinc gallium spinels. These nanoscale $ZnGa_2O_4$:Cu^{2+} spinels are obtained at low temperatures on a minute scale and the presented synthetic route furthermore offers different degrees of Cu-doping and morphology tuning options. The influence of the microwave treatment parameters on the chemical composition and the morphology of the mixed spinels was monitored with a wide repertoire of methods (electron microscopy including STEM/EDXS, LA-ICP-MS and magnetic measurements as well as UV/Vis spectroscopy). Note that it is very difficult to differentiate Zn, Cu and Ga with conventional X-ray diffraction methods so that we used element-specific methods to investigate the coordination environment of the Cu^{2+} ions within the $ZnGa_2O_4$ host matrix, namely X-ray absorption spectroscopy in terms of XANES (X-ray absorption near edge structure) and EXAFS (extended X-ray absorption fine structure) as well as electron paramagnetic resonance spectroscopy (EPR).[46–48]

Results and Discussion

Microwave-Hydrothermal Approach

In the following, the microwave-hydrothermal synthesis of $ZnGa_2O_4$:Cu^{2+} solid solutions is discussed in detail, because this innovative low-temperature method offers a convenient time- and energy-saving access to nanostructured spinels as advantages over other synthetic routes.[44,49] Although both gallium- and zinc-containing oxidic materials in particular have been efficiently synthesized through microwave-hydrothermal treatments (e.g. gallium zinc phosphate NTHU-4[6] and hierarchical ZnO nanostructures[50]), the synthesis of $ZnGa_2O_4$ as a technically relevant ternary oxide has never been pursued via this approach and little is known about its Cu^{2+}-doped nanoscale derivatives. Therefore, we have developed a process for tuning Cu^{2+}-containing $ZnGa_2O_4$ solid solutions starting from the readily available precursor materials $Ga_2(SO_4)_3{\cdot}xH_2O$, $ZnSO_4{\cdot}7H_2O$ and $CuCl_2{\cdot}2H_2O$.

Morphology and Composition

Microwave-assisted hydrothermal synthesis of Cu^{2+}-substituted $ZnGa_2O_4$ at 150 °C brings forward hierarchically structured spherical particles and agglomerates (cf. SEM images in Figure 1). Henceforth, we refer to the products as the $ZnGa_2O_4$:Cu^{2+}_n series with *n* representing the initial Cu^{2+} fraction (atom-%) of the total metal content (for further details on the preparation and the sample nomenclature cf. Exp. Section). The size of the individual $ZnGa_2O_4$:Cu^{2+} nanoparticle building units is as low as 10–20 nm (cf. Supporting Information, Figures S.1 and S.2). Only the sample with maximum initial copper content [denoted as $ZnGa_2O_4$:Cu^{2+}_25(12), with 12 indicating the number of vessels, cf. Exp. Section] consists of microspheres with an average diameter of approximately 1 μm (cf. Figure 2, a). Other than the remaining samples, this one was

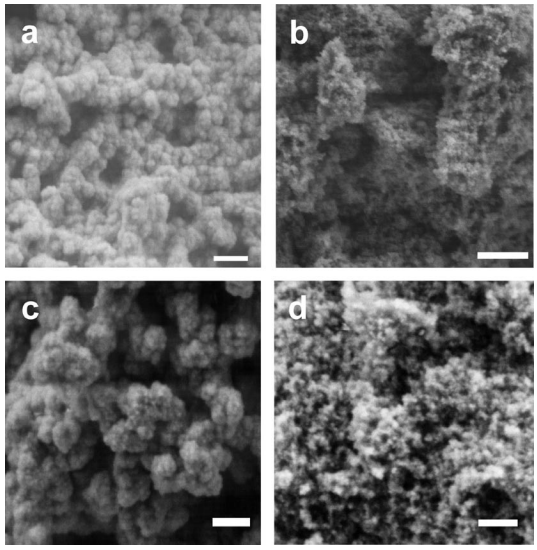

Figure 1. Representative SEM images of (a) $ZnGa_2O_4$:Cu^{2+}_25, (b) $ZnGa_2O_4$:Cu^{2+}_14, (c) $ZnGa_2O_4$:Cu^{2+}_4, (d) $ZnGa_2O_4$:Cu^{2+}_2 (scale bar: 200 nm).

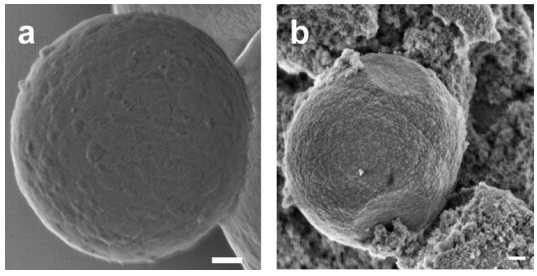

Figure 2. Representative SEM images of (a) $ZnGa_2O_4$:Cu^{2+}_25(12), (b) $ZnGa_2O_4$:Cu^{2+}_25_HY (scale bar: 200 nm).

synthesized using all 12 vessels of the microwave system simultaneously in order to investigate the scale-up options for zinc gallates with maximum copper contents as especially promising precursors for the fabrication of Cu-based nanocatalysts.[51] This morphology variation indicates that the load of the equipment is a key factor that has to be taken into account when employing microwave-hydrothermal reactors for large scale productions.

Interestingly, the analogous conventional-hydrothermal approach towards nanostructured Cu^{2+}-containing $ZnGa_2O_4$ failed to generate phase pure products with homogeneously distributed morphologies (Figure S.3 and Figure 2, b). This indicates the advantages of microwave-hydrothermal syntheses over the classic techniques in terms of shorter reaction times and homogeneous products.

The compositional homogeneity of the $ZnGa_2O_4$:Cu^{2+} mixed spinel series is confirmed by energy-dispersive X-ray (EDX) analyses that indicate constant ratios of Zn, Cu and Ga within a given sample (for a representative example cf. Figure 3). The overall elemental compositions of the zinc copper gallates were determined with state-of-the-art laser ablation inductively coupled plasma mass spectrometry (LA-ICP-MS). This highly sensitive analytical method permits advanced multi-element identification of a wide range of solid samples (e.g. geological and ceramic materials) and it is also a powerful tool for the characterization of otherwise insoluble nanostructured oxide materials. The unique combination of laser ablation and inductively coupled plasma as ionization source minimizes the experimental error due to the loss of volatile elements such as zinc.[52]

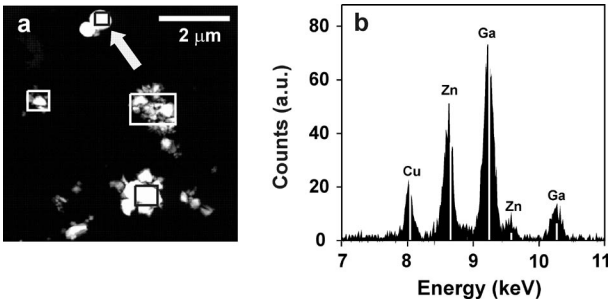

Figure 3. (a) STEM image (inset with spots indicating EDX analyses) and (b) representative EDX spot analysis of sample $ZnGa_2O_4$:Cu^{2+}_25(12).

The elemental compositions of microwave-hydrothermally synthesized Cu^{2+}-substituted $ZnGa_2O_4$ samples according to LA-ICP-MS analyses are summed up in Table 1 (for experimental parameters cf. Table S.2). Under the given microwave-hydrothermal conditions, we observed a maximum solubility of Cu^{2+} in the spinel lattice of ca. 5 atom-% (based on the metal content).

Table 1. Composition of the $ZnGa_2O_4$:Cu^{2+} solid solutions as determined from LA-ICP-MS analyses.

Sample	wt.-% Cu	wt.-% Zn	wt.-% Ga
$ZnGa_2O_4$:Cu^{2+}_14	3.5	21.9	48.5
$ZnGa_2O_4$:Cu^{2+}_4	1.1	23.7	49.7
$ZnGa_2O_4$:Cu^{2+}_2	0.6	23.7	49.5
$ZnGa_2O_4$:Cu^{2+}_1	0.4	24.1	48.9

Structural Investigations

The X-ray diffraction patterns recorded for the series of microwave-hydrothermally synthesized nanostructured Cu^{2+}-substituted $ZnGa_2O_4$ spinels are shown in Figure 4. All diffraction peaks can be indexed to the regular spinel structure of $ZnGa_2O_4$ (S.G. *Fd-3m*, cf. JCPDF No. 38-1240) and the diffraction patterns of the mixed spinels display a significant peak broadening, thereby confirming the nanostructuring of all samples.

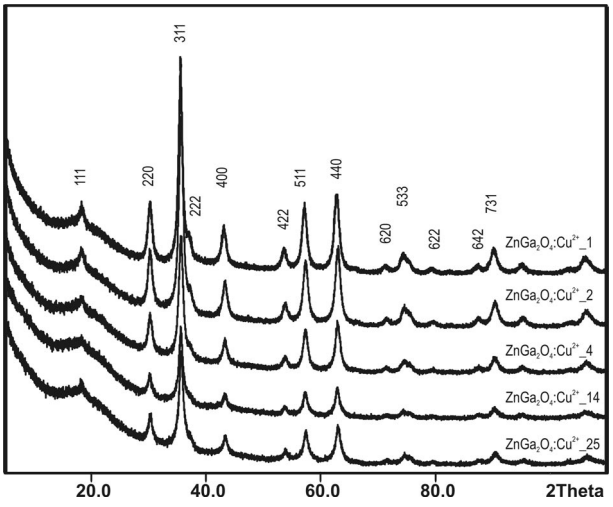

Figure 4. X-ray diffraction patterns of the Cu^{2+}-substituted $ZnGa_2O_4$ series synthesized with microwave-hydrothermal techniques.

Generally, the assignment of structural sites to guest ions in nanostructured solid solutions is important for tuning and understanding their properties, but this can become a demanding task. In the present case, X-ray diffraction investigations with Rietveld methods[53] regarding the localization of Cu^{2+} ions are further impeded by the similar scattering factors of copper, zinc and gallium so that the Rietveld refinement attempts failed to provide detailed information about the coordination environment of the individual cations. Table 2 shows that the lattice constants of all samples do not vary significantly with the copper content.

Table 2. Cell constants, cell volumes and FWHM values.

Sample	*a* /Å	V /Å^3	FWHM
$ZnGa_2O_4$:Cu^{2+}_25	8.342(1)	580.4	0.79
$ZnGa_2O_4$:Cu^{2+}_14	8.342(5)	580.5	0.71
$ZnGa_2O_4$:Cu^{2+}_4	8.340(6)	580.0	0.78
$ZnGa_2O_4$:Cu^{2+}_2	8.340(6)	580.1	0.82
$ZnGa_2O_4$:Cu^{2+}_1	8.340(4)	580.1	0.83

XANES and EXAFS are complementary tools to XRD in order to characterize the local electronic and geometrical environment of a target element in a crystalline or amorphous matrix in an element-specific manner. Therefore, we de-

termined the coordination of copper within the zinc gallate matrix with the help of these methods.

Figure 5 shows the background-subtracted and normalized XANES spectra recorded at the Cu *K*-edge of the CuO reference and of the $ZnGa_2O_4$:Cu^{2+}_4 and $ZnGa_2O_4$:Cu^{2+}_25(12) samples. It has been reported that the A and C resonances increase as B decreases with the reduction of the formal copper valency.[54,55] The XANES spectra of the samples $ZnGa_2O_4$:Cu^{2+}_4 and $ZnGa_2O_4$:Cu^{2+}_25(12) are quite similar (Figure 5, see related features A–C) and there is no indication for CuO segregation. Copper seems to be in an octahedral environment with an oxidation state +2, especially since comparable results have been observed in $CuFe_2O_4$-NiO nanocomposites.[56]

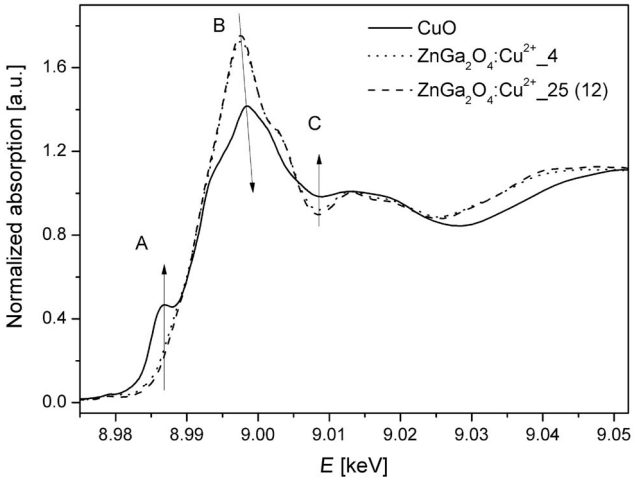

Figure 5. Cu *K* XANES spectra of the CuO reference and of the samples $ZnGa_2O_4$:Cu^{2+}_4 and $ZnGa_2O_4$:Cu^{2+}_25(12).

In order to obtain more in-depth structural information, EXAFS studies were performed on the $ZnGa_2O_4$:Cu^{2+}_25(12) sample. The Fourier transformed of the $k^3\chi(k)$ EXAFS data at the Cu *K*- and Zn *K*-edge are shown in Figure S.4 (without phase shift correction). The difference in the second shell shows clearly a difference in coordination geometry (cf. Figure S.4). The structural parameters deduced from the EXAFS data analysis are given in Table 3. For this purpose Cu was either placed on a tetrahedral or an octahedral site. Only the octahedral site resulted in reasonable fits at the Cu *K*-edge whereas Zn is mainly in tetrahedral geometry. Copper on a tetrahedral site resulted in too short Cu–Ga distances and an unreasonable energy shift. The fits can be improved assuming copper in a distorted octahedral environment, but this also increases the number of free fitting parameters.

EPR spectroscopy was performed on selected Cu^{2+}-substituted $ZnGa_2O_4$ samples to back the conclusions drawn from the EXAFS investigations. The CW-EPR X- and W-band spectra for Cu centers are shown in Figure 6. The spectra indicate the presence of a single type of Cu-centers with $g_{\|} = 2.34$, $A_{\|} = 0.0118\ cm^{-1}$ and $g_{\perp} = 2.07$. At higher doping levels the magnetic coupling between Cu-centers is

Table 3. Fit results at the Zn *K*-edge and Cu *K*-edge for the $ZnGa_2O_4$:Cu^{2+}_25(12) sample.[a]

Edge	Shell	Absorber	CN	*R* /Å	σ^2 /Å^{-2}	E_0 /eV	Res.
Zn *K*-edge	1	Zn-O	4*	1.99	0.011	–3.4	9.7
Tetrahedral Zn	2	Zn-Ga	12*	3.41	0.015	–5.5	
Cu *K*-edge	1	Cu-O	4*	1.94	0.007	–8.6	12.0
Assuming tetrahedral Cu	2	Cu-Ga	12*	3.19	0.012	–29.6	
Cu *K*-edge	1	Cu-O	6*	1.95	0.011	–8.6	12.1
Assuming octahedral Cu	2	Cu-Ga	6*	2.98	0.010	2.4	
Cu *K*-edge	1	Cu-O	3.4 (1)	1.95	0.006	–4.1	6.9
Assuming octahedral Cu	2	Cu-Ga/Cu	6*	2.99	0.010	1.2	
Cu *K*-edge	1	Cu-O	4*	1.97	0.007	–1.7	4.6
Assuming octahedral Cu	2	Cu-O	2*	2.25	0.014	6.7	
	3	Cu-Ga/Cu	6*	2.98	0.009	0.4	

[a] CN: number of neighbours, δ_i: Debye–Waller factor, R_i: interatomic distance, ΔE_i: energy difference (eV), Res.: residual; values labelled with an asterisk (*) were kept constant during the fit assuming $ZnGa_2O_4$ structure and copper replacing either the place of Zn or Ga.

observed which leads to the "exchange narrowed" line in the centre of the original uncoupled spectrum. Such large values of the parallel components of the *g*-tensor and hyperfine tensor are rather unusual for a Cu^{II} centre with tetrahedral coordination.[57]

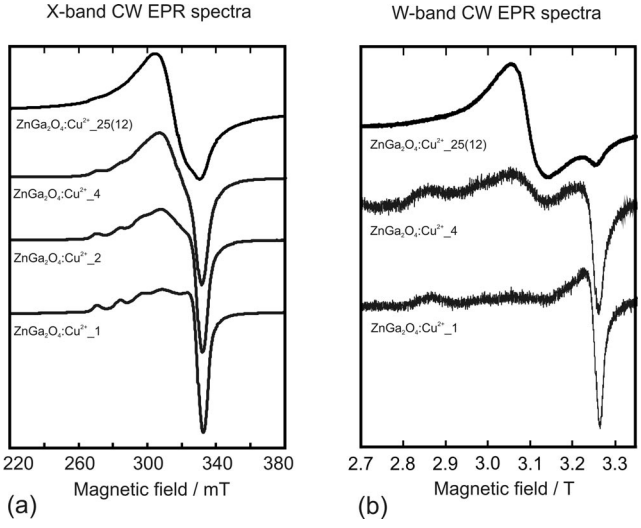

Figure 6. Room temperature CW EPR spectra for Cu-containing zinc gallate spinels with different copper concentrations: (a) X-band (9.87 GHz) and (b) W-band (94 GHz).

Nevertheless, the available EPR data on similar inorganic oxide systems rather imply that the observed species are Cu^{2+} ions in octahedral coordination. For copper-containing spinel solid solutions of the $Cu_xMg_{1-x}Al_2O_4$-type, the presence of Cu centers in both octahedral and tetrahedral environments has been observed with XPS and XRD.[58,59] The observed EPR spectra revealed *g*-values which are very close to the ones reported here ($g_{\|}$ = 2.32–2.35 and $g_{\perp}$ = 2.04–2.06).[58] The EPR active species were attributed to the

paramagnetic Cu-centers in a tetragonally-distorted octahedral coordination displaying Jahn–Teller distortion. In BeO and ZnO the EPR spectra of Cu^{2+} in tetrahedral coordination reveal *g*-values well below 2 in contrast to what we have observed ($g_{\parallel}$ = 0.74, $g_{\perp}$ = 1.531 for Cu/ZnO;[60] $g_{\parallel}$ = 1.709, $g_{\perp}$ = 2.379 for Cu/BeO[61]). The spectra could only be recorded at temperatures below 30 K, which is consistent with the measured *g*-values, as both phenomena can be interpreted in terms of strong admixing of the angular momentum to the spin state of copper. The observed hyperfine couplings were approximately two orders of magnitude smaller than the one reported here.

To summarize, we consider the observed EPR spectra to be due to the Cu^{2+} ions in a tetragonally distorted octahedral coordination. In principle, the presence of small amounts of tetrahedrally coordinated Cu-centers cannot be fully excluded, but they are not detectable at our experimental conditions. At the lowest available temperature (4 K) no additional EPR signal was observed in the field range corresponding to *g*-values from 0.75 to 3.0. For example, the relative fraction of the copper-centers in octahedral coordination was reported to decrease with the increase of the Cu content in the Mg/Al-spinel.[59] The EPR spectra are informative for the samples with substantially lower Cu content than those subjected to EXAFS investigations. For the samples with higher copper fractions, a single structureless EPR line was observed that is due to strong exchange coupling between different centers. This could also conceal possible EPR signals from Cu^{2+} in tetrahedral coordination.

It should furthermore be noted that in the samples with high density of copper centers both the hyperfine coupling to copper nuclei and the anisotropy of the *g*-tensor are averaged out in the EPR spectra. This implies either a distribution of the directions of tetragonal distortion within every single crystallite or a strong coupling between copper centers in different crystallites.

Materials Properties

The BET surface areas of the microwave-hydrothermally synthesized $ZnGa_2O_4$:Cu^{2+} spinel series are summarized in Table 4. Obviously, increasing copper contents lead to a decreasing surface area of the solid solutions. In comparison with literature data for the surface areas (12 and 37 m^2/g[12,62]), the pristine $ZnGa_2O_4$ obtained from microwave-assisted methods exhibits a significantly enhanced surface area of 63 m^2/g.

The solid solution series of Cu^{2+}-doped $ZnGa_2O_4$ spinels was furthermore characterized through UV/Vis spectroscopy. Obviously, the absorption edge displays a red shift with increasing copper contents in the spinel lattice (Table 5, Figure 7 and Figure S5). The according band gaps can be assigned through extrapolation of the absorbance edge to the wavelength axis. The value 4.3 eV of the pristine $ZnGa_2O_4$ is in line with the literature range of 4.4–5.0 eV.[7,12,25,63] The absorption maxima of the

Table 4. BET specific surface areas of $ZnGa_2O_4$:Cu^{2+} spinels.

Sample	BET [m^2/g]
$ZnGa_2O_4$:Cu^{2+}_25(12)	29 ± 2
$ZnGa_2O_4$:Cu^{2+}_25	65 ± 3
$ZnGa_2O_4$:Cu^{2+}_14	79 ± 4
$ZnGa_2O_4$:Cu^{2+}_4	72 ± 4
$ZnGa_2O_4$:Cu^{2+}_2	94 ± 5
$ZnGa_2O_4$:Cu^{2+}_1	100 ± 5
$ZnGa_2O_4$	63 ± 3

$ZnGa_2O_4$:Cu^{2+} series show a very slight tendency towards a blue shift with decreasing copper content that is not contradictory to the trends in individual particle sizes (Figure S.2) and BET surfaces (Table 4).

Table 5. Band gaps among the Cu^{2+}-doped $ZnGa_2O_4$ spinel series.

Sample	Peak position /nm	Band gap /eV
$ZnGa_2O_4$:Cu^{2+}_25	257	4.1
$ZnGa_2O_4$:Cu^{2+}_25(12)	253	4.3
$ZnGa_2O_4$:Cu^{2+}_14	254	4.3
$ZnGa_2O_4$:Cu^{2+}_4	245	4.5
$ZnGa_2O_4$:Cu^{2+}_2	245	4.4
$ZnGa_2O_4$:Cu^{2+}_1	245	4.4
$ZnGa_2O_4$	254	4.3

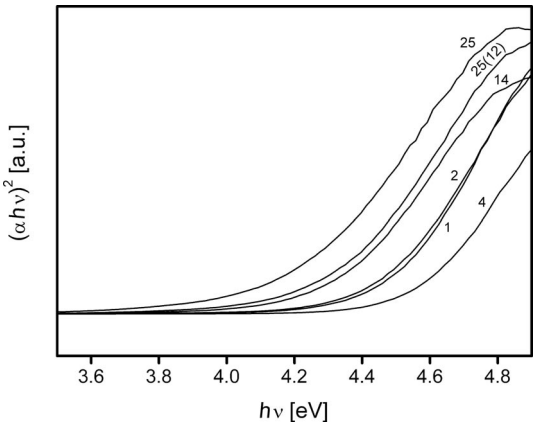

Figure 7. UV/Vis spectra of the nanostructured $ZnGa_2O_4$:Cu^{2+}_n mixed spinels (values of *n* are indicated at the respective curves).

Macroscopic support for the presence of Cu^{2+} in the spinel lattice stems from the temperature dependence of the magnetization *M*. The measurements were performed on two 30 mg powdered samples of $ZnGa_2O_4$:Cu^{2+} spinels with different copper contents ($ZnGa_2O_4$:Cu^{2+}_14 and $ZnGa_2O_4$:Cu^{2+}_1) in a magnetic field $\mu_0 H$ of 0.1 T. The data are presented in Figure 8, exhibiting a pronounced Curie dependence.

Deviations at high temperatures are due to the difficulty in probing the reduced magnetic moment in the magnetometer – this effect was especially pronounced in the less magnetic spinel sample with low copper content ($ZnGa_2O_4$:Cu^{2+}_1). The molar susceptibility $\chi_m = M/(Hn_{Cu})$ is calculated, taking the molar density n_{Cu} of copper

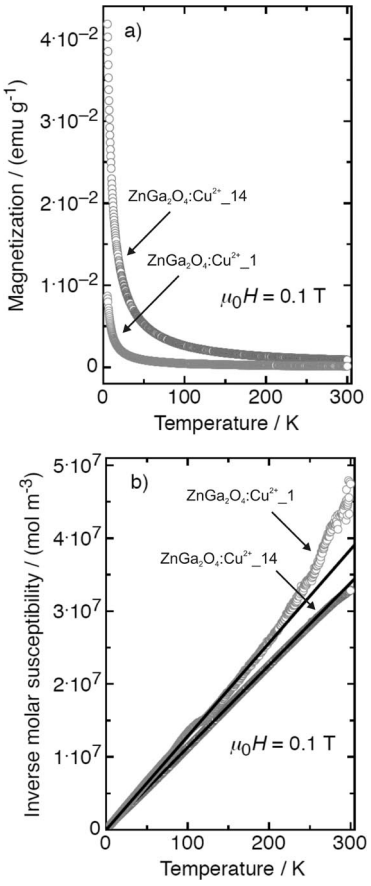

Figure 8. (a) Magnetization of two powder samples ($ZnGa_2O_4$:Cu^{2+}_14 and $ZnGa_2O_4$:Cu^{2+}_1) measured in 0.1 T magnetic field as a function of temperature; (b) derived inverse molar susceptibility from the magnetization data analyzed according to Equation (1), wherefrom the effective magneton number was calculated.

ions (derived from Table 2) into account. For estimating the effective magneton number p_{Cu} of the Cu^{2+} state, the molar susceptibility is analysed according to the Curie law

$\chi_m = (N_A\mu_0\mu_B^2/3k_BT)\ p_{Cu}$,

as described in ref.[46] As a result, p_{Cu} values of $p_{ZnGa2O4:Cu2+\_14}$ = 2.2(2) and $p_{ZnGa2O4:Cu2+\_1}$ = 2.1(2) are found for $ZnGa_2O_4$:Cu^{2+}_14 and $ZnGa_2O_4$:Cu^{2+}_1, respectively. They are in good agreement with the expected values for a free Cu^{2+} ionic state.

Conclusions and Outlook

The present study demonstrates that microwave-assisted hydrothermal methods offer an efficient access to nanostructured Cu^{2+}-containing $ZnGa_2O_4$ solid solutions. The homogeneous products are obtained within less than two hours of microwave synthesis with no further post-treatment requirements. Although the process is in principle scalable, the vessel load of the microwave reactor has to be carefully calibrated. Under the given microwave-hydrothermal conditions, the solubility of the copper ions in the spinel matrix reaches maximum values around 5 atom-%. The coordination environment of the Cu^{2+} ions has been investigated with a wide range of complementary analytical methods and their coordination can best be described as a tetragonally distorted octahedral environment. Microwave-hydrothermal methods are especially well suited for the nanoscale synthesis of ternary and higher oxide phase diagrams with volatile and redox-active components that are difficult to access with classic sintering methods. Therefore, a novel microwave-assisted synthesis of nanoscale $CuGa_2O_4$ as the other end member of the $ZnGa_2O_4$/$CuGa_2O_4$ solid solution series has also been developed and will be reported in due course. The main advantage of the newly presented synthetic approach is that these well-characterized nanostructured spinel materials are now available in larger quantities from a versatile protocol so that their sensor and photocatalytic properties will be investigated in more detail. Most importantly, the selective reduction of Cu^{2+} centers within the "redox-inert" $ZnGa_2O_4$ spinel matrix is currently being explored to generate novel catalysts with metal nanoparticles embedded into a structurally stable and well-defined environment. Furthermore, the present microwave-hydrothermal approach will be applied to other nanostructured spinel solid solutions with high application potential.

Experimental Section

General Synthesis: Gallium sulfate [$Ga_2(SO_4)_3{\cdot}xH_2O$, Aldrich, purity >99.995%], zinc sulfate ($ZnSO_4{\cdot}7H_2O$, Fluka, > 99.5%) and cupric chloride ($CuCl_2{\cdot}2H_2O$, Fluka, > 99%) were used without further purification. The starting materials with a metal ratio Zn/Ga of 1:2 and the different amounts of $CuCl_2{\cdot}2H_2O$ for the formation of solid solutions were dissolved in deionized water. The pH of the stirred solution was adjusted with aqueous ammonia (25% NH_3). All products were washed with deionized water, vacuum filtered and dried in air at 80 °C for 1 h. The initial copper content of the samples is indicated as follows in the sample nomenclature: $ZnGa_2O_4$:Cu^{2+}_n with *n* representing the atom-% of Cu^{2+} ions related to the total metal ion content.

Microwave-Hydrothermal Synthesis: The starting materials were mixed in a 95 mL CEM Omni Teflon® vessel and heated with a ramp to temperature mode within 30 min to 150 °C in a MARS5 microwave reactor (CEM Corporation) at 2.45 GHz and a power of 1600 W. If not otherwise mentioned, reactions were performed using five Teflon® vessels within one run with the $ZnGa_2O_4$:Cu^{2+}_25(12) sample being the only exception (simultaneous use of 12 vessels). The reaction temperature was kept constant for 1 h, followed by a 30 min cooling period. To control the pressure and temperature during the reaction, a reference vessel equipped with an appropriate sensor was used as well as IR sensors to monitor the temperature of all vessels. Overheating was prevented by constantly stirring the reaction mixture and automatic power adjustment to keep the temperature constant within a range of ± 5 °C.

Conventional-Hydrothermal Synthesis: All precursors were combined in a 23 mL stainless steel autoclave equipped with a Teflon® liner and heated at 180 °C for 48 h in a furnace (BINDER, FD 53).

Analytical Characterization: X-ray powder diffraction patterns (XRD) were recorded on a STOE STADI P diffractometer (trans-

mission mode, Ge monochromator) with Cu-$K_{\alpha 1}$ radiation. The morphology of the substances was examined using scanning electron microscopy performed on a LEO 1530 (FEG) microscope. Samples were dispersed in ethanol and applied on a silicon wafer. Determination of the metal ratios was performed with LA-ICP-MS methods. The analyses of the pressed powder samples were carried out using an 193 nm ArF excimer laser ablation system (Lambda Physik, Göttingen, Germany) coupled to an ICP-MS (DRC II +, Perkin–Elmer, Norwalk, USA). The samples were ablated for 40 s (5 Hz, 60 μm crater diameter) and the operating conditions are summarized in Table S.2. Furthermore, the molar ratio of Zn, Cu, and Ga was assigned with EDXS investigations performed on a Zeiss SUPRA 50 VP microscope equipped with an EDAX detector. For scanning transmission electron microscopy (STEM), the material was deposited on a perforated carbon foil supported on a molybdenum grid and investigated on a FEI CM30ST (LaB_6 cathode). In the STEM mode, the electron beam was placed on a selected areas, and an elemental analysis by energy-dispersive X-ray spectroscopy (EDXS, EDAX detector) was performed there. The specific surface area of the samples was investigated with an adsorption isotherm of nitrogen at 77 K based on the Brunauer–Emmett–Teller method (BET; Quadrasorb *SI*, Quantachrome). For UV/Vis spectroscopy investigations the samples were well mixed with $MgSO_4$ (water-free) by grinding and placed in a sample holder. The spectra were recorded using a Perkin–Elmer Lambda 750 spectrometer with an integrating sphere setup (diameter 110 mm). The samples were measured against pure $MgSO_4$ as reference within the wavelength range of 250–1000 nm. The applied diffuse reflectance spectra are transformed into absorption spectra using the Kubelka–Munk function. The continuous wave (CW) EPR spectra were measured at X-band with a Bruker ElexSys E500 spectrometer equipped with a ER 4122 SHQ resonator (Bruker Biospin, Germany, mw frequency 9.87 GHz). The W-band CW EPR measurements were recorded with a Bruker E680 spectrometer (Bruker Biospin, Germany, mw frequency 94 GHz). All EPR measurements were performed at room temperature.

Ex situ X-ray absorption spectroscopic data were recorded at beamline l811 at MAXLab (Lund, Sweden) using a Si(311) double crystal monochromator. The samples were pressed into self-supporting wafers with boron nitride and the Cu *K*- and Zn *K*-edge data were measured at 8.84–9.63 keV and 9.55 and 10.03 keV, respectively. All spectra were taken in transmission mode. XANES and EXAFS analysis was performed using Winxas 3.1[64] and phase and amplitude functions were calculated using the Feff-code.[65] To keep the systematic error in the data analyzing procedure at the same level all data were treated similarly. Pre-edge background subtraction and normalization was carried out by fitting a linear polynomial to the pre-edge region and a cubic polynomial to the post-edge region of the absorption spectra. A smooth atomic background, $\mu_0(k)$, was obtained through cubic polynomial. After background removal, the data were transformed into *k*-space. Fourier transforms (FT) of Cu *K*-edge $\chi(k)$ were multiplied by k^3, typically from 2.5–11.8 $Å^{-1}$; a Bessel-type window was used in the Fourier transform. The FEFF7 program package[66] was used to calculate phase and amplitude factors, followed by least-squares curve fitting of the data. The amplitude reduction factor was held constant to 0.87 (S_0^2), the value obtained from initial fits for a CuO FT EXAFS spectrum measured under the same experimental conditions. The error range of the S_0^2 was estimated as ± 0.01.

Magnetisation measurements were performed using a Quantum Design SQUID Magnetometer MPMS XL. The magnetic field strength of 0.1 T was applied upon zero-field cooling the sample and the magnetic moment of the sample was subsequently determined as a function of temperature.

Supporting Information (see also the footnote on the first page of this article): Detailed literature survey of $ZnGa_2O_4$ materials (Table S.1). TEM image of sample $ZnGa_2O_4$:Cu^{2+}_1 (Figure S.1). SEM images of selected $ZnGa_2O_4$:Cu^{2+} samples recorded at high magnifications (Figure S.2). XRD pattern of $ZnGa_2O_4$:Cu^{2+} obtained from conventional-hydrothermal synthesis (Figure S.3). Experimental parameters of LA-ICP-MS investigations (Table S.2). Fitting results of the Cu *K*-edge k^3-weighted EXAFS data at the Cu *K* and Zn *K*-edge of the $ZnGa_2O_4$:Cu^{2+}_25(12) sample (Figure S.4). UV/Vis spectra of $ZnGa_2O_4$:Cu^{2+} solid solutions (Figure S.5).

Acknowledgments

This work was supported by the Swiss National Science Foundation (SNSF) (Professorship PP002-114711/1), by the University of Zürich and the Graduate School of Chemical and Molecular Sciences Zürich (CMSZH). We acknowledge the support of the Electron Microscopy Center, ETH Zürich (EMEZ), and we are grateful to Dr. Frank Krumeich (EMEZ) for TEM investigations. The authors thank Dipl.-Chem. Claudia Rasch (Institute of Physical Chemistry, University of Potsdam) for UV/Vis spectroscopic measurements. Beamtime allocation at MAXLAB and financial support by the European Community – Research Infrastructure Action under the FP6: *Structuring the European Research Area* [*Integrating Activity on Synchrotron and Free Electron Laser Science* (IA-SFS) RII3-CT-2004-506008] and by the Danish Centre for the use of Synchrotron X-ray and Neutron facilities (DanScatt) is gratefully acknowledged.

[1] M. Niederberger, G. Garnweitner, N. Pinna, G. Neri, *Prog. Solid State Chem.* **2005**, *33*, 59–70.
[2] C. N. R. Rao, F. L. Deepak, G. Gundiah, A. Govindaraj, *Prog. Solid State Chem.* **2005**, *31*, 5–147.
[3] J. S. Kim, S. G. Lee, H. L. Park, J. Y. Park, S. D. Han, *Mater. Lett.* **2004**, *58*, 1354–1357.
[4] T. Minami, T. Maeno, Y. Kuroi, S. Takata, *Jpn. J. Appl. Phys. Part 2 - Lett.* **1995**, *34*, L684–L687.
[5] Y. S. Jeong, J. S. Kim, H. L. Park, *Solid State Commun.* **2006**, *139*, 157–160.
[6] J. A. Losilla, D. Coutinho, K. J. Balkus, *Microporous Mesoporous Mater.* **2008**, *113*, 325–332.
[7] X. Chen, H. Xue, Z. H. Li, L. Wu, X. X. Wang, X. Z. Fu, *J. Phys. Chem. C* **2008**, *112*, 20393–20397.
[8] W. Zhang, J. Zhang, Z. Chen, T. Wang, *Catal. Commun.* **2009**, *10*, 1781–1785.
[9] F. E. Osterloh, *Chem. Mater.* **2008**, *20*, 35–54.
[10] K. Ikarashi, J. Sato, H. Kobayashi, N. Saito, H. Nishiyama, Y. Inoue, *J. Phys. Chem. B* **2002**, *106*, 9048–9053.
[11] L. Pisani, T. Maitra, R. Valenti, *Phys. Rev. B* **2006**, *73*, 205204.
[12] S. Y. Bae, J. Lee, H. Jung, J. Park, J. P. Ahn, *J. Am. Chem. Soc.* **2005**, *127*, 10802–10803.
[13] J. S. Kim, J. S. Kim, T. W. Kim, H. L. Park, Y. G. Kim, S. K. Chang, S. Do Han, *Solid State Commun.* **2004**, *131*, 493–497.
[14] P. Dhak, U. K. Gayen, S. Mishra, P. Pramanik, A. Roy, *J. Appl. Phys.* **2009**, *106*, 063721 1–6.
[15] J. S. Kim, H. L. Park, *Solid State Commun.* **2004**, *131*, 735–738.
[16] J. J. Krebs, G. H. Stauss, J. B. Milstein, *Phys. Rev. B* **1979**, *20*, 2586–2587.
[17] T. Maitra, R. Valenti, *J. Phys.-Condes. Matter* **2005**, *17*, 7417–7431.
[18] Q. Shi, J. Y. Zhang, C. Cai, L. Cong, T. M. Wang, *Mater. Sci. Eng. B-Adv. Funct. Solid-State Mater.* **2008**, *149*, 82–86.

[19] Z. H. Xu, Y. X. Li, Z. F. Liu, Z. Xiong, *Mater. Sci. Eng. B-Solid State Mater. Adv. Technol.* **2004**, *110*, 302–306.
[20] S. H. Yang, M. Yokoyama, *Jpn. J. Appl. Phys. Part 1 - Regul. Pap. Short Notes Rev. Pap.* **1998**, *37*, 6429–6433.
[21] Y. Tang, Y. Liu, P. Zhu, Q. Xue, L. Chen, Y. Lu, *AIChe J.* **2009**, *55*, 1217–1228.
[22] L. Xu, Y. Su, Q. T. Zhou, S. Li, Y. Q. Chen, Y. Feng, *Cryst. Growth Des.* **2007**, *7*, 810–814.
[23] Z. Yu, H. Chen, Z. W. Li, Z. M. Yang, H. B. Song, Y. L. Gao, Y. S. Zhang, Y. Jin, Z. F. Jiao, M. Gong, J. G. Zhu, X. S. Sun, *Mater. Lett.* **2009**, *63*, 37–40.
[24] L. M. Chen, Y. N. Liu, Z. G. Lu, K. L. Huang, *Mater. Chem. Phys.* **2006**, *97*, 247–251.
[25] S. K. Sampath, J. F. Cordaro, *J. Am. Ceram. Soc.* **1998**, *81*, 649–654.
[26] J. S. Kim, H. L. Park, C. M. Chon, H. S. Moon, T. W. Kim, *Solid State Commun.* **2004**, *129*, 163–167.
[27] U. K. Gautam, Y. Bando, J. H. Zhan, P. Costa, X. S. Fang, D. Golberg, *Adv. Mater.* **2008**, *20*, 810–814.
[28] M. Cao, I. Djerdj, M. Antonietti, M. Niederberger, *Chem. Mater.* **2007**, *19*, 5830–5832.
[29] K. Sung, T. M. Chung, C. G. Kim, *Mater. Lett.* **2007**, *61*, 1011–1014.
[30] R. Reshmi, K. M. Krishna, R. Manoj, M. K. Jayaraj, *Surf. Coat. Technol.* **2005**, *198*, 345–349.
[31] G. R. Patzke, S. Locmelis, R. Wartchow, M. Binnewies, *J. Cryst. Growth* **1999**, *203*, 141–148.
[32] X. T. Zhang, Y. Y. Rao, Y. Liang, R. Deng, Z. Liu, S. Hark, Y. Yuen, S. P. Wong, *J. Phys. D: Appl. Phys.* **2008**, *41*, 095104.
[33] M. Hirano, *J. Mater. Chem.* **2000**, *10*, 469–472.
[34] M. Hirano, M. Imai, M. Inagaki, *J. Am. Ceram. Soc.* **2000**, *83*, 977–979.
[35] M. Hirano, N. Sakaida, *J. Am. Ceram. Soc.* **2002**, *85*, 1145–1150.
[36] Y. D. Li, X. F. Duan, H. W. Liao, Y. T. Qian, *Chem. Mater.* **1998**, *10*, 17–18.
[37] M. Rajamathi, R. Seshadri, *Curr. Opin. Solid State Mater. Sci.* **2002**, *6*, 337–345.
[38] K. Byrappa, M. Yoshimura, *Handbook of Hydrothermal Technology*, Noyes, Park Ridge, N. J., **2001**.
[39] R. Kiebach, N. Pienack, W. Bensch, J. D. Grunwaldt, A. Michailovski, A. Baiker, T. Fox, Y. Zhou, G. R. Patzke, *Chem. Mater.* **2008**, *20*, 3022–3033.
[40] A. Michailovski, M. Woerle, D. Sheptyakov, G. R. Patzke, *J. Mater. Res.* **2007**, *22*, 5–18.
[41] G. R. Patzke, F. Krumeich, R. Nesper, *Angew. Chem. Int. Ed.* **2002**, *41*, 2446–2461.
[42] M. Schaefer, D. Kurowski, A. Pfitzner, C. Naether, Z. Rejai, K. Moller, N. Ziegler, W. Bensch, *Inorg. Chem.* **2006**, *45*, 3726–3731.
[43] S. Baldassari, S. Komarneni, E. Mariani, C. Villa, *J. Am. Ceram. Soc.* **2005**, *88*, 3238–3240.
[44] S. Komarneni, H. Katsuki, *Pure Appl. Chem.* **2002**, *74*, 1537–1543.
[45] G. Buhler, A. Zharkouskaya, C. Feldmann, *Solid State Sci.* **2008**, *10*, 461–465.
[46] A. Le Nestour, M. Gaudon, G. Villeneuve, R. Andriessen, A. Demourgues, *Inorg. Chem.* **2007**, *46*, 2645–2658.
[47] A. Le Nestour, M. Gaudon, G. Villeneuve, M. Daturi, R. Andriessen, A. Demourgues, *Inorg. Chem.* **2007**, *46*, 4067–4078.
[48] M. Robbins, L. Darcy, *J. Phys. Chem. Solids* **1966**, *27*, 741–743.
[49] A. Sonnauer, N. Stock, *J. Solid State Chem.* **2008**, *181*, 3065–3070.
[50] P. L. Zhu, J. W. Zhang, Z. S. Wu, Z. J. Zhang, *Cryst. Growth Des.* **2008**, *8*, 3148–3153.
[51] M. Behrens, *J. Catal.* **2009**, *267*, 24–29.
[52] D. Guenther, B. Hattendorf, *Trac-Trends Anal. Chem.* **2005**, *24*, 255–265.
[53] H. M. Rietveld, *J. Appl. Crystallogr.* **1969**, *2*, 65–71.
[54] D. Grandjean, H. L. Castricum, J. C. van den Heuvel, B. M. Weckhuysen, *J. Phys. Chem. B* **2006**, *110*, 16892–16901.
[55] T. Vitova, J. Hormes, K. Peithmann, T. Woike, *Phys. Rev. B* **2008**, *77*, 10.
[56] R. K. Selvan, V. Krishnan, C. O. Augustin, H. Bertagnolli, C. S. Kim, A. Gedanken, *Chem. Mater.* **2008**, *20*, 429–439.
[57] J. R. Pilbrow, *Transition Ion Electron Paramagnetic Resonance*, Clarendon Press, Oxford, **1990**.
[58] P. K. Sharpe, J. C. Vickerman, *J. Chem. Soc., Faraday Trans. I* **1977**, *73*, 505–513.
[59] J. S. D. Vinuela, C. O. Arean, *Phys. Status Solidi A - Appl. Res.* **1987**, *101*, 57–61.
[60] R. E. Dietz, H. Kamimura, A. Yariv, M. D. Sturge, *Phys. Rev.* **1963**, *132*, 1559–1569.
[61] M. Dewit, A. R. Reinberg, *Phys. Rev.* **1967**, *163*, 261–265.
[62] V. R. Kumar, K. V. Narasimhulu, N. O. Gopal, H. K. Jung, R. P. S. Chakradhar, J. L. Rao, *J. Phys. Chem. Solids* **2004**, *65*, 1367–1372.
[63] L. Zou, X. Xiang, M. Wei, F. Li, D. G. Evans, *Inorg. Chem.* **2008**, *47*, 1361–1369.
[64] T. Ressler, *J. Synchrot. Radiat.* **1998**, *5*, 118–122.
[65] M. Newville, *J. Synchrot. Radiat.* **2000**, *8*, 322–324.
[66] A. L. Ankudinov, J. J. Rehr, *Phys. Rev. B* **1997**, *56*, R1712–R1715.

Received: December 2, 2009
Published Online: March 25, 2010

